Chinese Journal of Chemical Engineering 79 (2025) 219–233

Contents lists available at ScienceDirect

Chinese Journal of Chemical Engineering

journal homepage: www.elsevier.com/locate/CJChE

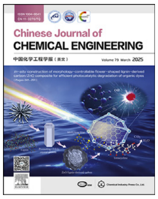

Full Length Article

Effects of noise on fluidized bed characteristics measurements by electrical capacitance tomography

Kai Huang [1,2,3], Chunlei Pei [2], Shuanghe Meng [3], Wuqiang Yang [4], Hua Li [3], Mao Ye [3,5,*], Jinlong Gong [1,2,*]

[1] Joint School of National University of Singapore and Tianjin University, International Campus of Tianjin University, Binhai New City, Fuzhou 350207, China
[2] Key Laboratory for Green Chemical Technology of Ministry of Education, School of Chemical Engineering and Technology, Collaborative Innovation Center of Chemical Science and Engineering, Tianjin University, Tianjin 300072, China
[3] Dalian National Laboratory for Clean Energy and National Engineering Laboratory for MTO, Dalian Institute of Chemical Physics, Chinese Academy of Sciences, Dalian 116023, China
[4] Department of Electrical and Electronic Engineering, The University of Manchester, Manchester M13 9PL, UK
[5] Tianjin Normal University, Tianjin 300387, China

ARTICLE INFO

Article history:
Received 10 May 2024
Received in revised form
17 September 2024
Accepted 18 September 2024
Available online 9 January 2025

Keywords:
Noise
Electrical capacitance tomography
Fluidized bed
Signal-to-noise ratio
Measurement

ABSTRACT

Noise is inevitable in electrical capacitance tomography (ECT) measurements. This paper describes the influence of noise on ECT performance for measuring gas–solids fluidized bed characteristics. The noise distribution is approximated by the Gaussian distribution and added to experimental capacitance data with various intensities. The equivalent signal strength (ϕ) that equals the signal-to-noise ratio of packed beds is used to evaluate noise levels. Results show that the Pearson correlation coefficient, which indicates the similarity of solids fraction distributions over pixels, increases with ϕ, and reconstructed images are more deteriorated at lower ϕ. Nevertheless, relative errors for average solids fraction and bubble size in each frame are less sensitive to noise, attributed to noise compromise caused by the process of pixel values. These findings provide useful guidance for assessing the accuracy of ECT measurements of multiphase flows.

1. Introduction

Electrical capacitance tomography (ECT) is a non-intrusive visualization tool for inspecting multi-phase flows, such as gas–liquid, gas–liquid–solids, and gas–solids fluidized beds [1–3]. Owing to its non-radiative, non-invasive, fast-speed and cost-effective properties, ECT has found widespread use in various processes. Generally, ECT measurements aim to reconstruct the permittivity distribution or material distribution from capacitance data obtained using non-iterative or iterative algorithms [4,5]. However, this process often suffers from under-determined and ill-conditioned problems. The former arises from the limited number of independent measurements, leading to alternative images, while the latter results from the non-uniformity in the sensitivity matrix and makes the reconstructed image easily affected by capacitance perturbations (*i.e.*, noise effects), which requires a higher signal-to-noise ratio (SNR) system [4,6]. Several studies have focused on improving the capacitance acquisition system to increase capacitance measurement resolution [7–11]. For instance, an AC-based capacitance circuit system with the digital switching demodulator achieved a 60 dB SNR level for 500 fF (1 fF=1×10^{-15} F) capacitance measurement, corresponding to a system resolution of 0.5 fF [8]. Similarly, Kryszyn *et al.* [7] developed a single-shot, high-voltage circuit system with a 30 dB SNR level for 2.5 fF capacitance measurement, resulting in a system resolution of 0.06 fF. Al Hosani *et al.* [9] employed a commercial PTI300E-TP-G capacitance measurement system, enabling them to collect data with an effective resolution of 0.1 fF. Despite these efforts to enhance the SNR of capacitance acquisition systems, noise remains inevitable due to non-ideal electronic elements, thermal effects on the resistor, and signal source fluctuations [7], which significantly limits the capacitance measurement resolution.

As previously mentioned, noise is an inherent factor in ECT measurements, and its noise intensity is determined by the acquisition system and the magnitude of the measured capacitance, as the calibration procedure uses the capacitance difference between media [4]. For instance, Li and Holland [12] employed a data acquisition system with the Gaussian noise measuring 1 fF,

---

* Corresponding authors.
E-mail addresses: maoye@dicp.ac.cn (M. Ye), jlgong@tju.edu.cn (J. Gong).

https://doi.org/10.1016/j.cjche.2024.09.033

resulting in a peak SNR of 40 dB based on the change in capacitance. Their study showed that the impact of noise on capacitance measurements increases with the distance between electrode pairs due to the reduction in capacitance difference between low and high calibration states. Zeeshan *et al.* [13] proposed a new measurement strategy that employed partially overlapping constituent segments from synthetic electrodes, which were sequentially activated. They demonstrated that the SNR increases with the number of combined small electrode sensors. Previous research verified that when measuring bubble-related parameters in fluidized beds with a fixed electrode width, the length of the ECT electrode should be minimized as much as possible [14]. However, an ECT sensor with a shorter electrode length (given a fixed width) will yield a smaller capacitance value and change, thus amplifying the noise effect. Additionally, the capacitance difference decreases with the reduction in permittivity difference between materials used in the low and high calibration procedures, further increasing the noise effect on the normalized capacitance measurements. Therefore, the effect of noise on ECT measurements varies based on the ECT sensor configuration and measurement conditions.

Previous studies have investigated the impact of noise on ECT measurements [15–17]. Wang *et al.* [15] added 40 dB and 60 dB noise to capacitance in their gas–oil two-phase flow simulation study. They found that data with 60 dB noise did not affect image quality, while data with 40 dB noise degraded the images. However, it is necessary to clarify whether the measurement of characteristics of the two-phase flow structure is impeded under the influence of 40 dB noise. Xie *et al.* [16] added 20 dB and 30 dB Gaussian white noise to four typical two-phase flow models and compared the similarity and value difference between reconstructed images with and without noise effects using two parameters, *i.e.*, correlation coefficient and image error, to evaluate the noise effect. Their results demonstrated that the combined algorithm (*i.e.*, a combination of the Landweber and Tikhonov algorithms) improved image quality compared with the Tikhonov algorithm. Liu *et al.* [17] designed an ECT sensor with internal electrodes to visualize a large-scale concentric-annulus zone, achieving an SNR of approximately 50 dB with different R_1/R_2 (*i.e.*, outer diameter/inner diameter) of the sensor. Their findings indicated that noise impacted reconstructed images under this SNR level. Although previous studies qualitatively evaluated the impact of noise on ECT measurements, the quantitative evaluation of its effects has not been reported, which can introduce uncertainties.

This study aims to simulate the impact of noise, commonly in ECT measurements, on reconstructed images and other characteristics of fluidized beds, compared to those obtained without noise interference under specific algorithms. Firstly, we added noise with various intensities to the normalized capacitance data obtained from fluidized bed measurements using 8 and 12-electrode ECT sensors. Subsequently, we computed reconstructed images with different noise levels and analyzed the effect of noise on the reconstructed images compared to noise-free images using statistical methods. Specifically, the influences of noise on the measurements of solids fraction over pixel and frame and the bubble size are analyzed in detail. Our study quantitatively identifies the noise effect on ECT characterization, offering guidance for designing and applying ECT technology, especially for measuring fluidized bed characteristics.

2. Methodology

2.1. Capacitance data acquisition

The measurements of capacitance data were obtained from specially designed apparatuses, as shown in Fig. 1, which include three different internal diameters (*i.e.*, 45, 55, and 65 mm) fluidized beds equipped with the 8 or 12-electrode ECT sensor with the same electrode length of the columns. The superficial gas velocity was gradually increased from the packed bed regime to the turbulent bed regime. A detailed description can be found in our previous study [14].

2.2. Noise distribution and application method

In ECT measurements, a normalized capacitance vector with either 28 or 66 elements is obtained when exciting each electrode of the 8 or 12-electrode sensor, respectively. Each element represents a measurement from one electrode pair comprising true value and noise. The noise distribution of each electrode pair was determined by analyzing normalized capacitance vectors obtained from packed bed measurements, where variations in normalized capacitance were assumed to be only related to noise. The measurement error (λ_n) of each electrode pair induced by noise was calculated by subtracting the average value, regarded as the true value, from the measured normalized capacitance, as shown in Eq. (1).

$$\lambda_n = \lambda_{ns} - \lambda_s \tag{1}$$

where λ_{ns} represents the measured normalized capacitance with the effect of noise for one electrode pair, and λ_s denotes the average normalized capacitance value across all frames from one electrode pair.

Fig. 2 displays the typical probability distributions of noise for 8-electrode and 12-electrode ECT sensors in the packed bed. These results demonstrate that the noise can be approximated by a Gaussian distribution. The width of the distribution is related to the SNR, which signifies the ratio between the desired signal and the background noise, as given in Eq. (2) [18,19].

$$\mathrm{SNR} = 20\ \mathrm{lg}\left(\frac{\mathrm{Signal}}{\mathrm{Noise}}\right) = 20\ \mathrm{lg}\sqrt{\frac{\sum_{i=1}^{Q} \lambda_{ns}(i)^2}{\sum_{i=1}^{Q} \left(\lambda_{ns}(i) - \overline{\lambda}_{ns}\right)^2}} \tag{2}$$

where $\lambda_{ns}(i)$ is the normalized capacitance with the noise effect of *i*th frame for one electrode pair measurement, $\overline{\lambda}_{ns}$ is the average value of all measured frames of one electrode pair (*i.e.*, λ_s), and Q is the total number of frames (20000 in this study). Similar Gaussian distributions with varying SNRs were also observed in other electrode pairs.

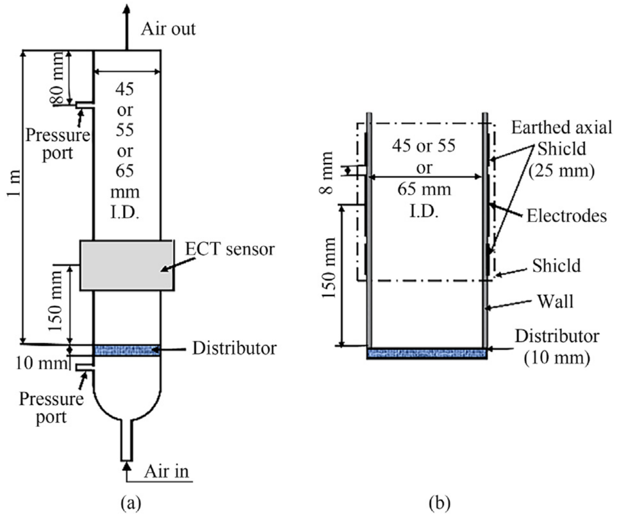

Fig. 1. (a) Schematic illustration of the fluidized bed set-up and (b) vertical view of the ECT sensor.

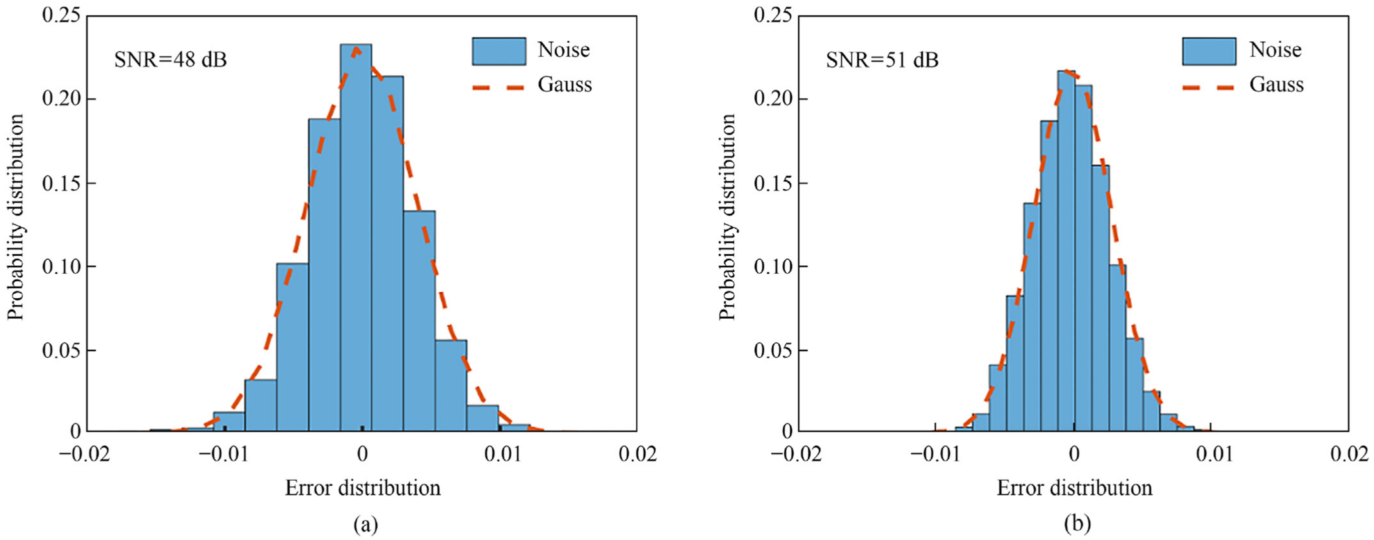

(a) (b)

Fig. 2. Typical probability distributions of noise in (a) 8-electrode ECT sensor and (b) 12-electrode ECT sensor.

We verified the stability of noise in ECT measurements. This was achieved by comparing the standard deviation of measured normalized capacitance in the homogeneous fluidization regime of a fluidized bed filled with catalyst particles used in the fluid catalytic cracking process (abbreviated as FCC particles) [20]. In this regime, the bed experiences homogeneous expansion without fluctuations of solids fraction. Thus, we observed that the measured capacitance decreases as the solids fraction decreases, and the fluctuations in capacitance are solely attributed to noise due to the homogeneous distribution of solids fraction. Fig. S1(a) (in Supplementary Material) shows the variation in the standard deviation of the measured normalized capacitance of different electrode pairs against time-averaged normalized permittivity (*i.e.*, time-averaged solids fraction) using an 8-electrode ECTsensor. The stable standard deviations of normalized capacitance vectors for each electrode pair indicate a consistent noise level (as shown in Eq. (2)) without being affected by the signal level induced by the change in normalized permittivity (solids fraction) for each electrode pair, ranging from 0.9 to 1. Additional studies involving the insertion of tubes with different diameters into a packed bed further confirmed that the noise level remains unchanged with variations in the solids fraction distribution (Fig. S1(b)). Therefore, as a working assumption, we consider that the noise follows a Gaussian distribution and remains stable in highly fluctuating systems. The impact of dynamic factors, such as the presence of moving bubbles in the bubbly flow regime and solids fraction fluctuations in turbulent and fast flow regimes, on noise level will be investigated further in future studies. It should also be noted that our objective is to examine the impact of noise on ECT performance, particularly concerning the normalized permittivity distribution of each frame, which is accomplished by introducing noise with different intensities to the measured data. Once the noise in the gas—solids fluidized bed is determined, our study enables the evaluation of measurement accuracy.

As the stability of the noise level in the measurements is assumed, we can add noise to the measured values according to Eq. (3), a variant of Eq. (1).

$$\lambda_{\text{ns}} = \lambda_{\text{s}} + N\left(0, \sigma^2\right) \tag{3}$$

where λ_{s} is the measured data, regarded as true values, $N(0, \sigma^2)$ is Gaussian distributed represents the noise (λ_{n}) with a mean of 0 and a standard deviation of σ.

Given the simplicity of obtaining the SNR in the fixed bed regime and the difficulty in obtaining the SNR during the fluidization process due to consistent variations in capacitance measurements with fluidization states, we can use the SNR of the packed bed to calculate the noise level of the measurement system. Therefore, we define the equivalent signal strength (ϕ), which equals the SNR of packed beds, to evaluate the noise level, as the signal in packed beds is unified. As λ_{ns} is assumed to be 1 in the packed bed, we can obtain the relationship between ϕ and σ according to Eq. (2), as shown in Eq. (4),

$$\phi = 20\ \lg\left(\frac{1}{\sigma}\right) \tag{4}$$

Thus, we change Eq. (3) to Eq. (5),

$$\lambda_{\text{ns}} = \lambda_{\text{s}} + N\left(0, 10^{-\phi/10}\right) \tag{5}$$

This approach ensures that the results can directly assess the performance of ECT measurements, given that ϕ equals the SNR value of the packed bed according to Eq. (2).

Furthermore, our analyses indicate that although there is a significant difference in the standard capacitance between adjacent and non-adjacent pairs, this does not affect the noise levels of each electrode pair due to the application of the AC-based measurement circuit [21]. We verified it using two methods.

On one hand, we directly obtained and analyzed the raw capacitance. We utilized another sampling device from the School of Electrical and Information Engineering, Tianjin University, based on an AC-based circuit, to measure the raw capacitance and noise directly, given that our device can only access the normalized capacitance [21,22].

Due to the minimal changes in capacitance, a normalization process is necessary to improve the quality of the reconstructed images [4]. Therefore, the normalized capacitance is calculated according to Eq. (6).

$$\lambda = \frac{C - \overline{C_{\rm L}}}{\overline{C_{\rm H}} - \overline{C_{\rm L}}} \tag{6}$$

where $\overline{C_{\rm L}}$ and $\overline{C_{\rm H}}$ represent the mean raw capacitance vectors for all electrode pairs in the low and high-permittivity calibration procedures, *i.e.*, the empty and fixed phases, respectively, and keep constant in the measurement. With the packed bed, the measured capacitance (C) can be written in Eq. (7).

$$C = C_{\rm H} + \sigma(C_{\rm H}) \tag{7}$$

where $\sigma(C_{\rm H})$ represents the standard deviation of $C_{\rm H}$. Thus, Eq. (6) can be simplified to Eq. (8).

$$\lambda = 1 + \frac{\sigma(C_{\rm H})}{\overline{C_{\rm H}} - \overline{C_{\rm L}}} \tag{8}$$

Therefore, the first and second terms on the right side of the equation can be interpreted as the signal and noise components, respectively. Fig. S2(a) presents the capacitance changes (represented by the voltage changes) for empty and fixed beds and the standard deviation of capacitance (represented by the measured voltage) in the fixed bed state, along with SNRs based on the normalized capacitance measurements in a specific sensor (diameter: 45 mm; electrode length: 45 mm). The figure shows their SNR values are similar, indicating that the magnitude is independent of the electrode pair's position because the raw capacitance's standard deviation and the capacitance difference between the calibration states exhibit the same trend.

The observed trend results from the circuit design, which amplifies the capacitance difference between calibration states to the same analog-to-digital converter (ADC) range, thereby inducing consistent changes in capacitance differences and noise, as shown in Eq. (8) and Fig. S2(a). Further details can be found in their work.

On the other hand, if the noise measured using Eq. (8) is related to the position of the electrode pairs, sensors with the same structure should exhibit similar variation patterns in the SNR of the electrode pairs at different positions due to the consistency in relative positioning. We further compared the SNRs of three sensors with similar structures but varying sizes, as shown in Fig. S2(b). Details of the sensor configurations and measurement conditions are provided in Table S1. The figure does not show that the SNR follows specific distribution patterns among the various electrode pairs.

However, the SNR values for different electrode pairs can vary significantly for specific sensors, as shown in Fig. S2(b). According to Eq. (8), this variation is likely due to the differences in the values of $C_{\rm H}$ and $C_{\rm L}$ between different electrode pairs, which are influenced by sensor structure measurement medium, and other environmental considerations. During the measurement process, the difference signal ($C - \overline{C_{\rm L}}$) is amplified. When this difference is minimal, the impact of measurement errors is amplified, leading to different SNRs for different electrode pairs. Conversely, the noise level decreases as the difference increases, resulting in a higher SNR and lower noise intensity. This is demonstrated in Fig. S2(c), which shows the capacitance changes ($\overline{C_{\rm H}} - \overline{C_{\rm L}}$) and the corresponding SNR values for two different sensors. This observation supports the analysis discussed earlier.

Consequently, we introduced noise with the same level across all electrode pairs to facilitate a more generalized discussion. This approach allows scenarios with varying noise levels across different channels when using the maximum noise level as the benchmark. Since the noise distribution with a higher ϕ is encompassed within that of a smaller ϕ, as ϕ is related to the Gaussian distribution width according to Eq. (4). Moreover, further studies could build upon this work to evaluate the impact of noise using a specific noise distribution.

We introduced noise by varying ϕ from 10 to 70 dB in 2 dB increments, following Eq. (5).

2.3. Evaluation procedures

Detailed procedures to evaluate the effect of noise on the reconstructed images of fluidized beds are outlined below. Firstly, randomly selected ECT measurement data from the packed bed to the turbulent bed with 8-electrode and 12-electrode sensors is regarded as reference data. Here, we should note that all selected data inherently includes noise. However, the successful application of ECT in gas–solids fluidized bed measurements demonstrates that noise does not entirely obliterate the capacitance measurements [2,3]. Since the average solids fraction of each frame corresponds to capacitance measurements, from the packed bed to the slugging bed (Fig. 3), we also present the composition of each frame based on its average solids fraction across all 50000 frames in the 8-electrode ECT measurements, as shown in Fig. S3. The figure shows many frames fall within the packed bed regime, with the solids fraction of the packed bed set to 0.63. All frames were obtained from the laboratory batch fluidized beds, using silica particles as the fluidization medium, with a minimum fluidization velocity of 4.8 $\rm cm\cdot s^{-1}$. The maximum superficial gas velocity is 30 $\rm cm\cdot s^{-1}$, and we collected data from 0 to 30 $\rm cm\cdot s^{-1}$. During the measurement process, smaller intervals were used initially, resulting in more frames in the fixed bed regime. The frame distribution in the 12-electrode ECT measurements is consistent with the results shown in Fig. S3. Furthermore, this study focuses on comparing the similarity and value difference in solids fraction distributions between the reference data and derived data with various noise intensities. Therefore, the original noise itself will not affect the findings of this study. In addition, the measurement frequency of the 8-electrode ECT sensor is around 90 Hz as well as 70 Hz for the 12-electrode ECT sensor in this study. In previous studies, several studies have evaluated the fluidized bed characteristics in the frequency domain [23–26]. Their results showed the typical frequency in the gas–solids fluidized beds is below 10 Hz, which indicated that the ECT measurement frequency can capture fluidized bed characteristics across the bubbling regime to the fast fluidization regime. Secondly, the Gaussian-distributed noise with various noise levels (10–70 dB, at 2 dB intervals) is added to each electrode pair measurement of each frame data from the first step, which ensures that noise is added coherently. Thirdly, the same algorithms are used to reconstruct normalized permittivity distributions. Finally, fluidized bed characteristics at various noise levels are derived from the reconstructed solids fraction distributions, allowing for the assessment of noise impact on ECT characterizations.

Reconstructed algorithms, which fall into non-iterative and iterative categories, are crucial for ECT measurements [4,5]. Non-iterative algorithms, such as linear back-projection (LBP) and Tikhonov regulation algorithms, offer online but low-quality images. Iterative algorithms, including Landweber iteration and simultaneous iterative reconstruction algorithms, provide high-quality images but require longer reconstruction time [4,5]. To study the effect of noise on fluidized bed characteristics measurements under different algorithm types, four algorithms are employed: the non-iterative linear back-projection; the non-iterative modified Tikhonov with the regularization parameter of 0.005 (MT-0.005); the simultaneous iterative reconstruction algorithm with the relaxation factor of 0.2 and iteration numbers of 10 (SIRT-0.2-10); and the adaptive projected Landweber iteration algorithm with 200 iteration numbers (APLI-200) [4,14,27,28].

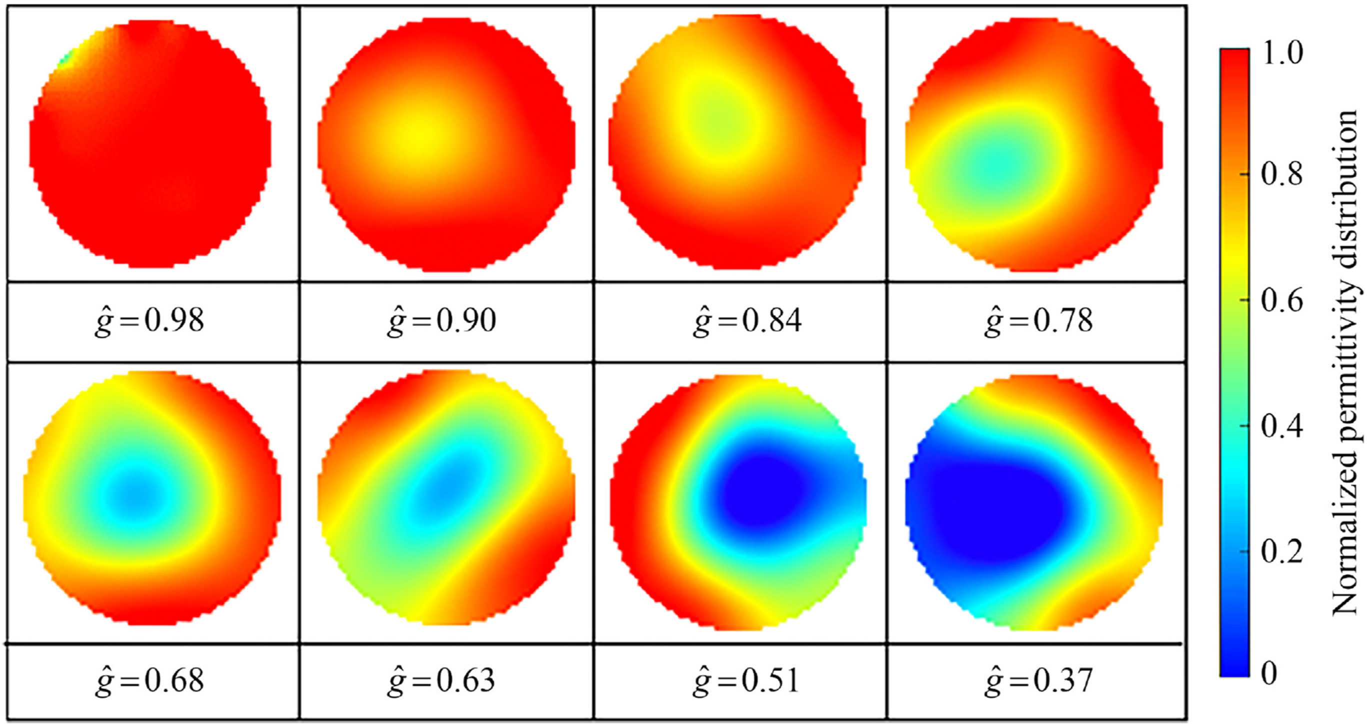

Fig. 3. Typical solids fraction distributions corresponding to the chosen normalized capacitance vectors, from the packed bed to the slugging bed. $\hat{g}$ is the average normalized permittivity for each frame.

In this work, we evaluate the impact of noise on the characteristics of the fluidized bed based on the reconstruction process using a specific sensor with a 65 mm inner diameter and a 2 mm thick wall. The structure of ECT sensors can affect the sensitivity distributions, and changes in sensitivity distribution can have implications for noise effects. Parameters such as electrode number, electrode-to-gap ratio, and sensor thickness play a role in shaping sensitivity distributions. According to a study by Fang *et al.* [26], the electrode-to-gap ratio of our sensor (8, which is greater than 6) ensures that it has no significant effect on the sensitivity distribution. Previous research has demonstrated that increasing sensor wall thickness can distort the sensitivity distribution of adjacent electrode pairs [29,30]. In other words, the greater wall thickness reduces the level of sensitivity for capacitance measurements, resulting in reduced noise effects. This finding is supported by the computation of the condition number of the related matrix. In this study, we utilized the LBP algorithm for obtaining results, and the outcomes obtained from other algorithms were like those obtained using the LBP algorithm. Thus, we can analyze the influence of wall thickness on noise effects by computing the condition number of the transpose matrix of the sensitivity distribution according to the LBP algorithm, as illustrated in Fig. S4 [4]. As depicted in the figure, an increase in wall thickness/outer diameter leads to a decrease in the condition number, indicating a reduction in the influence of capacitance perturbation. We obtained results using a ratio of 0.029, implying that the findings can be potentially applied to sensors with large wall thickness/outer diameter concerning relevant process conditions.

2.4. Parameters computation

Once the normalized permittivity distribution is reconstructed, different fluidized bed characteristics can be calculated. Eq. (9) calculates the average normalized permittivity for each frame, which is the basis for computing fluidized bed characteristics.

$$\widehat{g} = \frac{\sum_{i=1}^{N} g_i \times s_i}{\sum_{i=1}^{N} s_i} \tag{9}$$

where $\widehat{g}$ is the average normalized permittivity of each frame, g_i is the normalized permittivity of ith pixel, s is the area of each image pixel, and N is the number of pixels, which is 3228 in this work.

After obtaining the average normalized permittivity of each frame, the average solids fraction of each frame can be calculated by multiplying it by the average solids fraction of the packed bed, as shown in Eq. (10),

$$\widehat{\beta} = \widehat{\theta} \cdot \widehat{g} \tag{10}$$

where $\widehat{\beta}$ is the average solids fraction of each frame, and $\widehat{\theta}$ is the average solids fraction of the packed bed. Because packed bed solids fractions depend on particle diameter distribution, sphericity, and so on, we set the average solids fraction of the packed bed to 1. This does not influence the measurement results as per Eqs. (11) and (12) and facilitates the comparison of normalized permittivity distributions.

Upon obtaining the solids fraction distribution for a frame, the Pearson correlation coefficient (r), defined in Eq. (11), measures the similarity between solids fraction distributions with and without noise over pixels for a frame [16].

$$r = \frac{\sum_{i=1}^{N} \left(\beta_{\text{noise},i} - \widehat{\beta}_{\text{noise}}\right)\left(\beta_i - \widehat{\beta}\right)}{\sqrt{\sum_{i=1}^{N} \left(\beta_{\text{noise},i} - \widehat{\beta}_{\text{noise}}\right)^2} \cdot \sqrt{\left(\beta_i - \widehat{\beta}\right)^2}} \tag{11}$$

β and β_{noise} denote the solids fraction distributions with and without noise over pixels, respectively, and N is the number of pixels, *i.e.*, 3228 in this work.

After obtaining the average solids fraction of each frame, the relative error between average solids fractions with and without noise can be calculated using Eq. (12),

$$\widehat{\beta}_{\mathrm{re}} = \frac{\left|\widehat{\beta}_{\mathrm{noise}} - \widehat{\beta}\right|}{\widehat{\beta}} \times 100\% \tag{12}$$

where $\widehat{\beta}_{\mathrm{re}}$ is the relative error (*i.e.*, the value difference between solids fraction distributions) with and without noise [16].

3. Results and Discussion

3.1. The effect of noise on solids fraction distributions

ECT can visualize the internal permittivity distribution of a gas—solids reactor [3,14,23,27]. As shown in Eq. (11), the Pearson correlation coefficient was computed to assess the similarity between solid fraction distributions without and with varying noise levels. Fig. S5 illustrates the changes in Pearson correlation coefficient distributions concerning ϕ for the 8-electrode ECT sensor measurements. The number of sample data points can influence the Pearson correlation coefficient distribution. Therefore, 50000 Pearson correlation coefficient data points, spanning from the packed bed regime to the slugging regime, were used to determine how many samples are enough to eliminate statistical error. As a result, we compared the ratio of Pearson correlation coefficients greater than 0.99 with different numbers of samples.

Fig. 4 shows the relationship between the ratio of Pearson correlation coefficients greater than 0.99 and the number of samples, as determined by the LBP algorithm. The results indicate that the ratio remains stable when there are 5000 or more samples. Consequently, a sample size of 5000 was deemed sufficient, and the ratio value can be regarded as the probability. Fig. 4 reveals that the ratio of Pearson correlation coefficients exceeding the same threshold (*i.e.*, >0.99) increases with ϕ, indicating a reduction in noise impact, which will be further discussed. Similar results were obtained for different Pearson correlation coefficients.

Fig. 5 displays the probability against ϕ for different Pearson correlation coefficient limits based on 8-electrode ECT sensor measurements and various algorithms. The sample size was set to 50000. As the Pearson correlation coefficient increases, Fig. 5 demonstrates that ϕ also increases for the same probability, indicating a higher requirement for noise restriction. Additionally, the necessary ϕ for different algorithms increases in the order of LBP, MT-0.005, SIRT-0.2-10, and APLI-200 for the same Pearson correlation coefficient requirements. This is due to the propagation of measurement errors as algorithm complexity increases, especially when comparing LBP and APLI-200 algorithms. Because the results from the APLI-200 algorithm are based on those obtained from the LBP algorithm and include an additional 200 iterations, the measurement error induced by noise is amplified, consequently leading to a higher ϕ requirement. Similar trends were observed for the 12-electrode ECT sensor, as shown in Fig. S6. Moreover, Tables S2 and S3 show the necessary ϕ for the Pearson correlation coefficient to exceed the designed thresholds with a 0.995 probability, representing the required SNRs of the packed bed for ECT measurements. These values are greater than 58 dB, showing a strict requirement for the ECT measurement system.

Fig. 6 shows representative reconstructed images with different ϕ using the 8-electrode ECT sensor to reflect the relationship among the noise, Pearson correlation coefficient, the relative error of average solids fractions, and characterized solids fraction distribution. Similar results for the 12-electrode ECT sensor are shown in Fig. S7. Fig. 6 and Fig. S7 reveal that the similarity between reconstructed images with and without noise effect increases with the increase of ϕ. Fig. 6 also demonstrates that the impact of noise on reconstructed images decreases when the bed is fluidized. This is attributed to the fluctuation of the original normalized capacitance distribution (*i.e.*, the original solids fraction distribution) induced by the hydrodynamic effect of fluidized beds. As shown in Fig. 6, when the average normalized permittivity distribution approaches

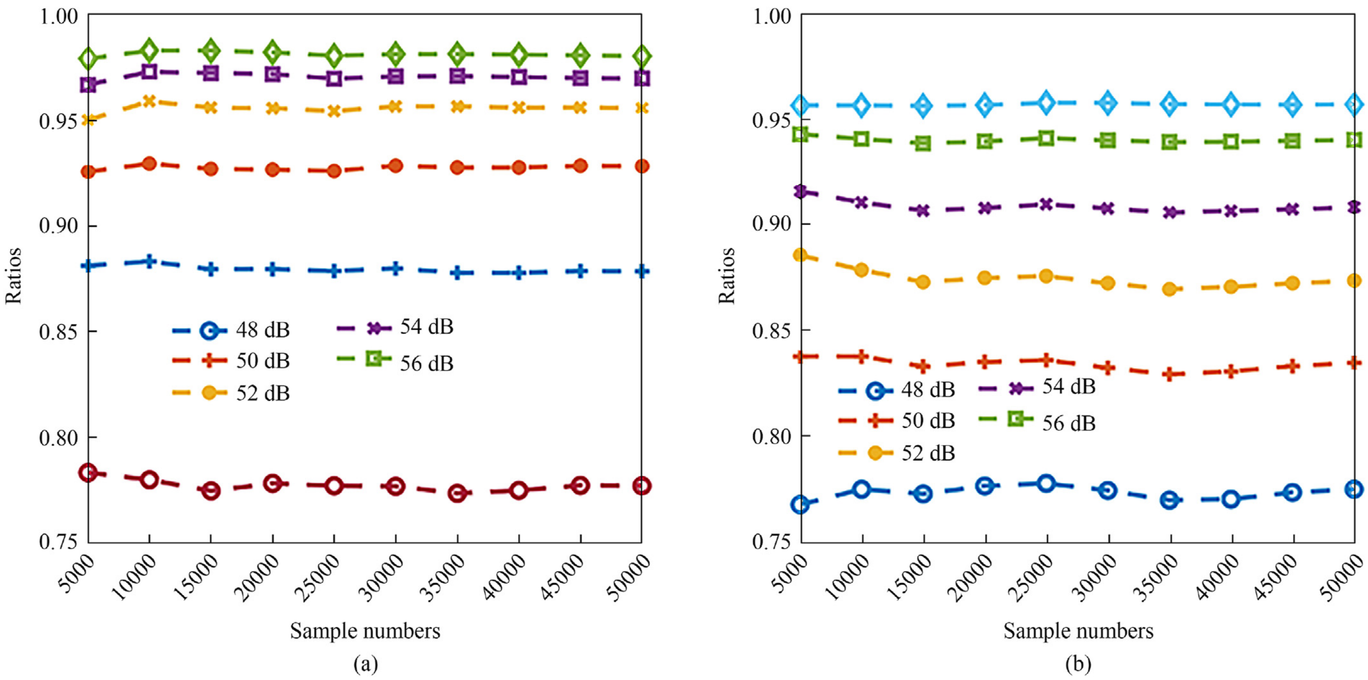

(a) (b)

Fig. 4. Fluctuations in the ratio of Pearson correlation coefficients that exceed 0.99 with different sample sizes, as determined by the LBP algorithm: (a) 8-electrode ECT sensor, (b) 12-electrode ECT sensor.

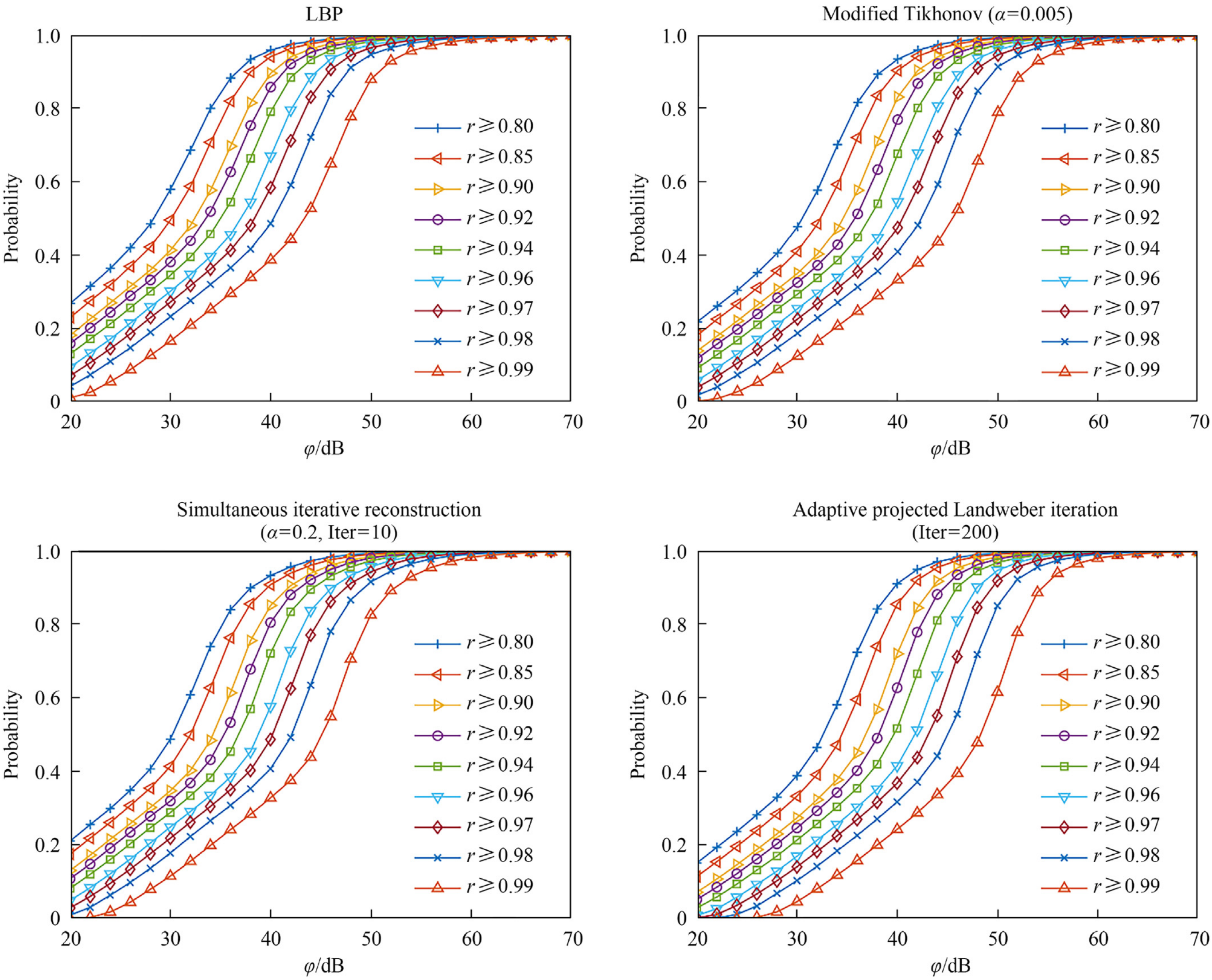

Fig. 5. Changes in the probability of ensuring Pearson correlation coefficients are greater than designed thresholds with ϕ, with the 8-electrode ECT sensor and four algorithms.

1, the normalized permittivity distribution over pixels presents minimal fluctuation. Consequently, noise induces noticeable distortion in the reconstructed image. Conversely, when a bubble is present in the reconstructed image, noise has a limited impact on image distortion. We further visually demonstrate the relationship between the impact of noise and the fluctuation in solids fraction distribution in Fig. S8. Fig. S8(a) shows the normalized permittivity distribution across pixels with and without noise effects in both the packed bed and fluidized bed regimes, illustrating how fluctuations reduce the impact of noise. Fig. S8(b) presents the relationship between the standard deviation of the normalized permittivity distribution (representing fluctuation) and the Pearson correlation coefficients for 248 samples at the same noise level. Generally, the Pearson correlation coefficient increases with the standard deviation of normalized permittivity distribution in a frame, further supporting the above discussion.

Fig. 7 shows the requirements of ϕ that ensure a probability greater than 0.995 for various Pearson correlation coefficient thresholds with the designed limitation of average normalized permittivity using the 8-electrode ECT sensor measurements and different algorithms. The figure presents that the required ϕ decreases as the bed is fluidized with a relatively low average normalized permittivity (*i.e.*, average solids fraction). This observation aligns with the preceding discussion, attributing it to the fluctuation of the original normalized permittivity distribution induced by the hydrodynamic effect of fluidized beds. Similar results were obtained with the 12-electrode ECT sensor, as shown in Fig. S9. Additionally, when the probability is designed to exceed 0.999, the ϕ requirements change little for both 8-electrode and 12-electrode ECT measurements, as shown in Figs. S10 and S11.

It is necessary to clarify that the results in Fig. 5 and Fig. S6 depend on the data we selected. The number of frames with different average solids fractions will impact the distributions in Fig. 5 and Fig. S6. This is because the similarity of the solids fraction distributions with and without the noise effect is related to the average solids fraction, as indicated in Fig. 7 and Fig. S9. When we reduce the frames in the fixed bed regime, the statistical results become more resistant to noise overall, causing the curves in Fig. 5 and Fig. S6 to shift to the left.

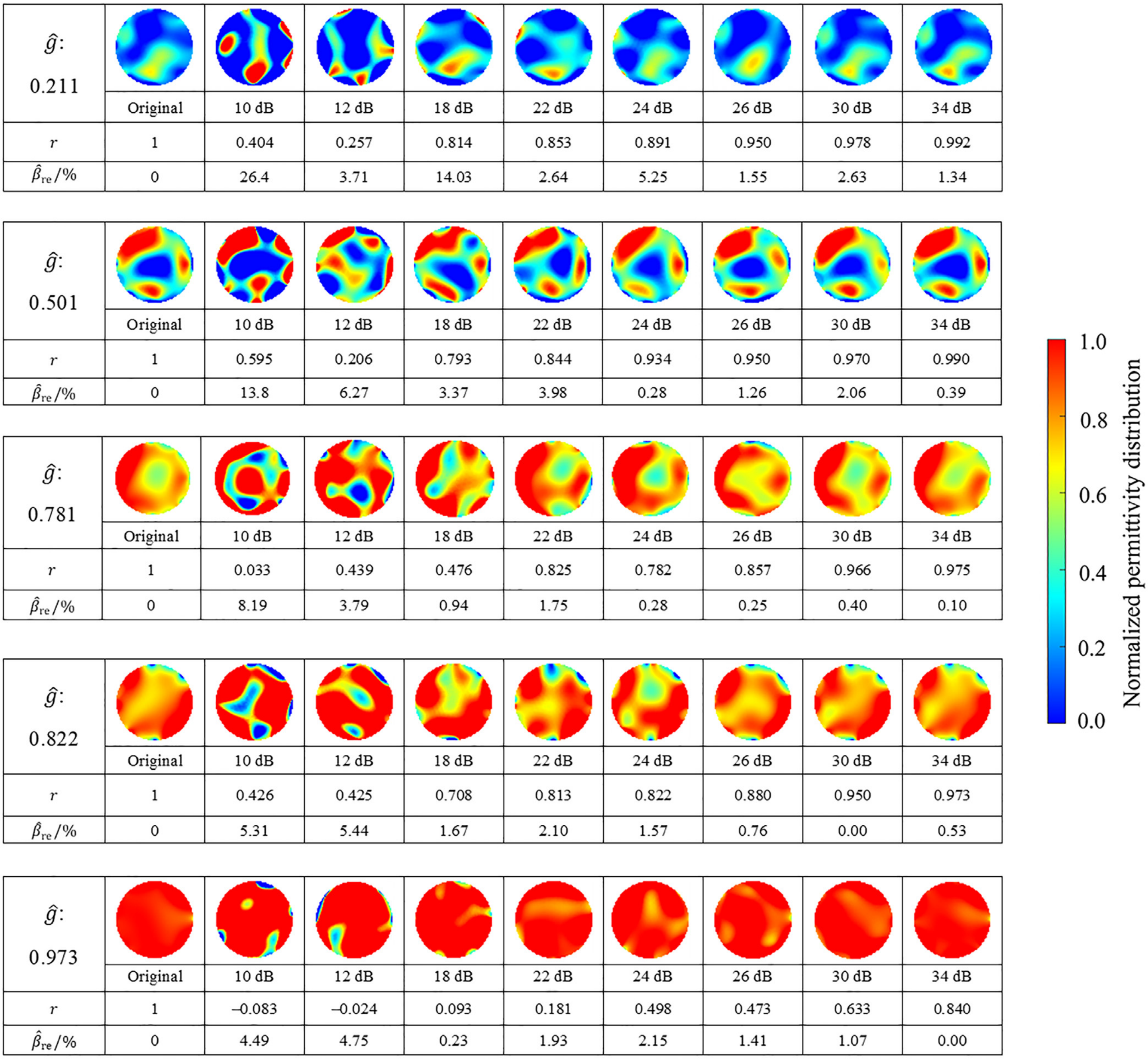

Fig. 6. Six reconstructed images with varying ϕ, with the 8-electrode ECT sensor and the adaptive projected Landweber algorithm (Iteration = 200). $\hat{g}$ represents the average normalized permittivity of the original frame, r is the correlation coefficient, and $\hat{\beta}_{re}$ denotes the relative error.

3.2. The effect of noise on the average solids fraction of each frame

Figs. 6 and S7 also present the relative error of average solids fractions ($\hat{\beta}_{re}$, the value difference between solids fraction distributions) with and without noise impact. These figures show that as the SNR increases, the impact of noise on the relative error of the average solids fraction rapidly decreases, even when the Pearson correlation coefficient does not meet the designed requirement. It can also be observed that the influence of noise is independent of the average solids fraction. This suggests that the impact of noise on accurately measuring the average solids fraction of each frame differs from its impact on accurately measuring the solids fraction distribution.

Fig. 8 presents the probabilities of the relative error of the average solids fraction of each frame being below pre-specified thresholds against ϕ for 8-electrode ECT measurements, obtained from 50000 data sets with different algorithms. Similar results were obtained with the 12-electrode ECT sensor, as shown in Fig. S12. These results suggest that ϕ, ensuring the same probability, increases with the decrease in the relative error of average solids fractions, indicating a reduction in noise effect. Additionally, as shown in Fig. 6 and Fig. S7, we found that the impact of noise on the relative error of average solids fractions is independent of the algorithm used, which can be attributed to relative error and average solids fraction independence. To further illustrate this, Fig. 9 presents reconstructed images with identical noise levels across four

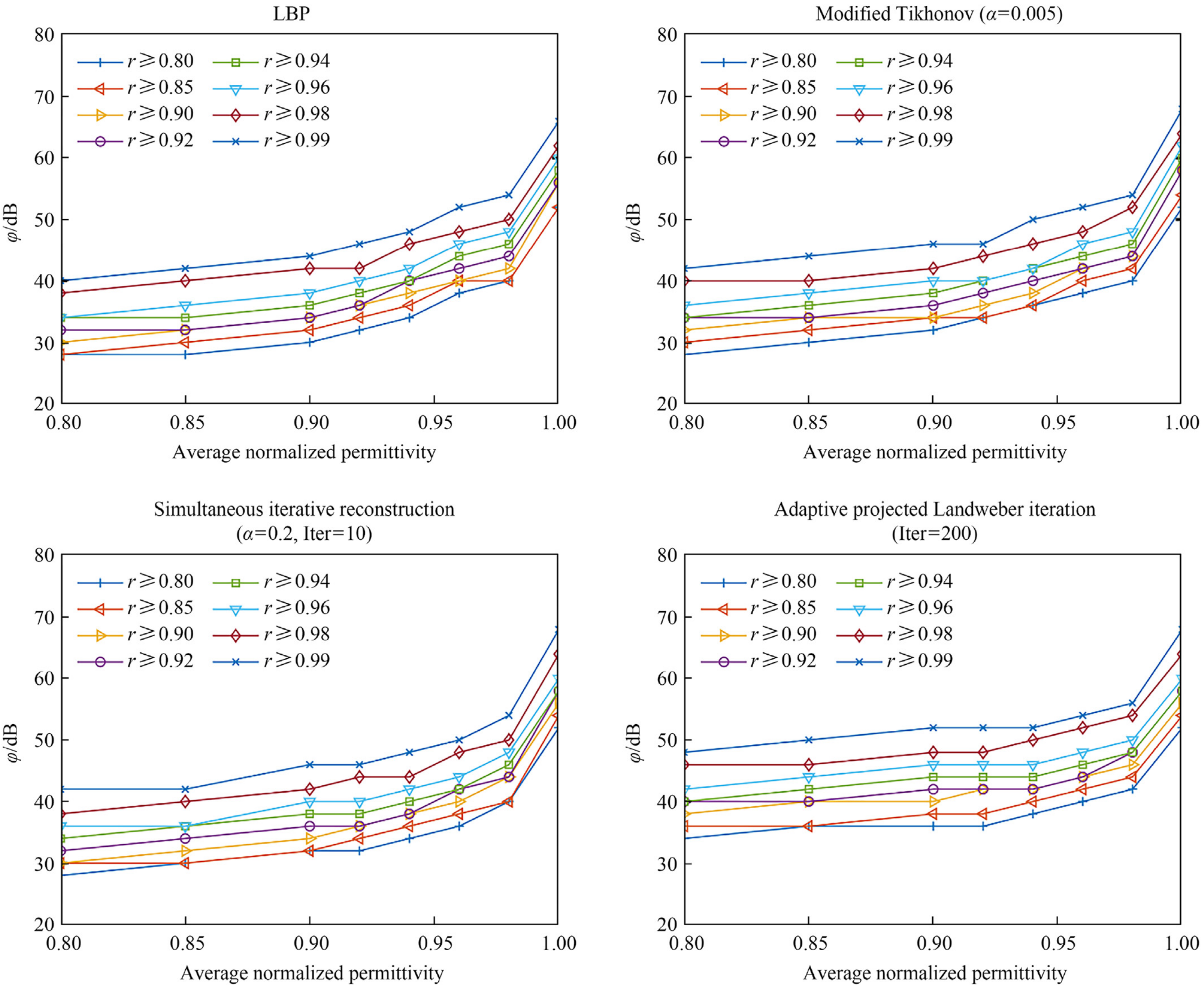

Fig. 7. Changes in ϕ that ensure the probability (Pearson correlation coefficient > designed thresholds) is greater than 0.995 with the designed limitation of average normalized permittivity, with the 8-electrode ECT sensor and four algorithms.

algorithms based on a single ECT measurement. Furthermore, when comparing the results measured with the 8-electrode and 12-electrode ECT sensors, the noise effect on the average solids fraction seems more pronounced with the 8-electrode ECT sensor than with the 12-electrode ECT sensor. This is likely because more capacitance values are obtained from the 12-electrode ECT measurements, decreasing the uncertainty when reconstructing the normalized permittivity distributions.

Tables S4 and S5 provide additional results of the required ϕ that ensure a probability greater than 0.999 for the relative error to be smaller than the pre-specified threshold. The results show that the required ϕ values for comparing the relative error of the average normalized permittivity of each frame are lower than those for comparing the Pearson correlation coefficient of normalized permittivity distributions, as shown in Tables S2 and S3. For instance, Table S6 shows the corresponding Pearson correlation coefficients that ensure the same probability when the relative error threshold is specified. As seen in Table S6, the corresponding correlation coefficients are smaller than the required values. Consequently, a higher ϕ, representing a stricter noise restriction, is required when comparing the similarity of solids fraction distributions. This phenomenon occurs because the fluctuations in the solids fraction of individual pixels induced by noise are counteracted when calculating the average solids fraction for each frame. This is confirmed by examining the distribution of errors in the solids fractions of 3228 pixels in one frame, as depicted in Fig. S13. The distribution illustrates that errors are alleviated when averaging all pixel values.

3.3. *The effect of noise on single-pixel value measurements*

The solid fraction over each pixel is important as it determines the dynamic flow pattern [24]. Therefore, evaluating the noise effect on pixel values is crucial. As shown above, we have discussed the noise effect on the average solids fraction of each frame using the relative error of average solids fractions as a parameter, as described in Eq. (12). Similarly, we also studied the noise effect on the single pixel value based on the relative error of the solids fraction of individual pixel with and without noise. We analyzed 50000 frame data sets, and each frame contains 3228-pixel values. Fig. 10 presents the probabilities of the relative error of solids fraction for each pixel being below pre-specified thresholds against

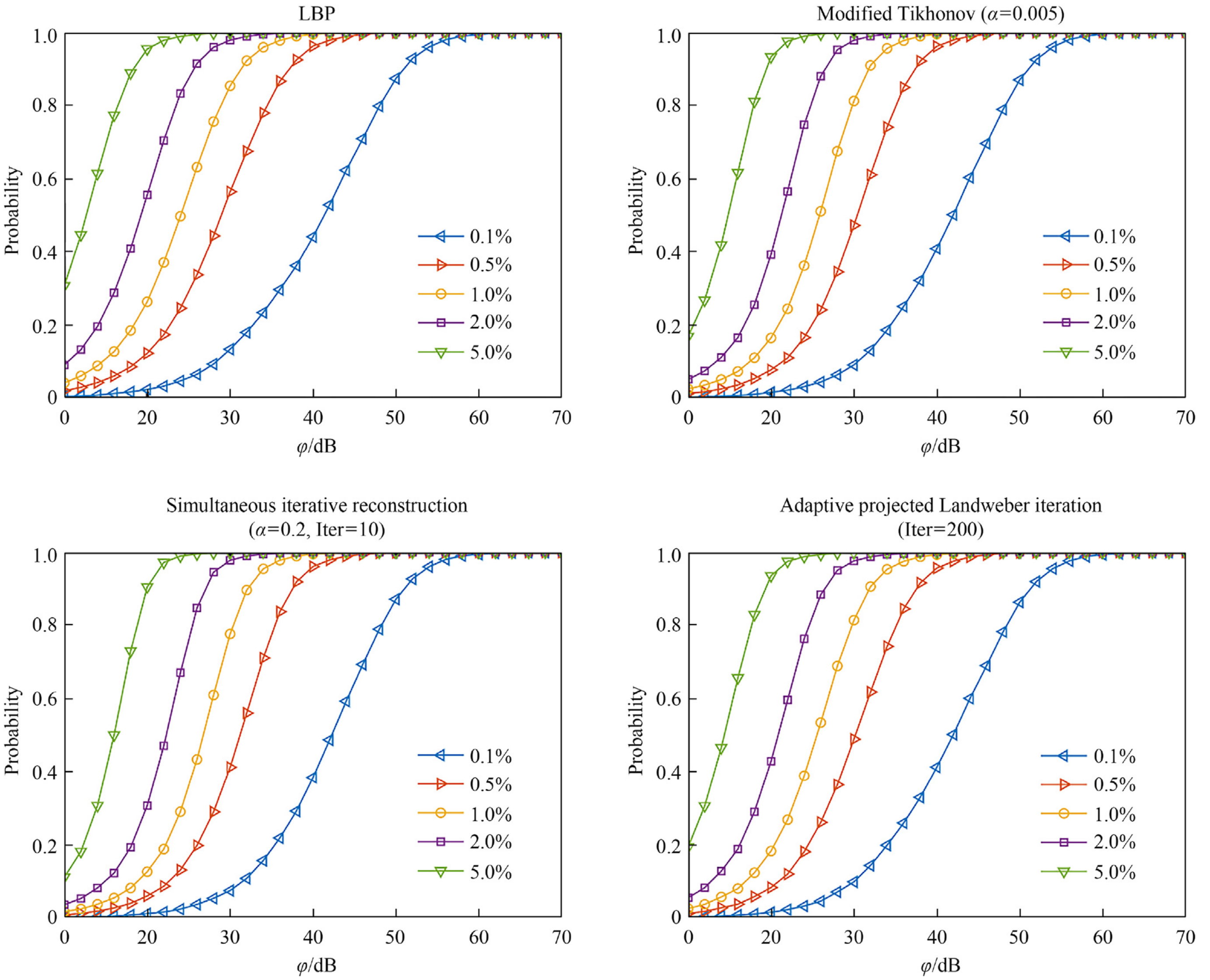

Fig. 8. Changes in the probability of ensuring the relative error of frame-based average solids fraction is smaller than designed thresholds with ϕ, with the 8-electrode ECT sensor and four algorithms.

ϕ for 8-electrode ECT measurements. It should be emphasized that the noise effect on the frame average solids fraction is mitigated by averaging pixel values, while pixel solids fraction measurements require higher ϕ. For instance, with 40 dB of ϕ, the probability of achieving a relative error of frame-based average solids fraction smaller than 2% exceeds 0.999, while the probability of achieving a relative error of pixel-based solids fraction smaller than 2% exceeds 0.974 for the 8-electrode ECT measurements with the LBP algorithm. In addition, we included the results obtained with the 12-electrode ECT sensor in Fig. S14. It is also found that the noise effect appears to be more sensitive for the 8-electrode ECT sensor than for the 12-electrode ECT sensor due to the decrease in uncertainty when reconstructing the normalized permittivity distributions by the 12-electrode ECT sensor. Additionally, we found that the impact of noise does not exhibit a clear trend with the locations or solids fraction values. Fig. S15 presents four typical solids fraction distributions and corresponding relative error distributions obtained using the 12-electrode sensor and the adaptive projected Landweber algorithm. To ensure consistency in our plots, we normalized the relative error with the maximum value of each corresponding frame. This approach does not alter the distribution of the relative error. As shown in Fig. S15, the relative error distribution appears random across the pixels and does not exhibit a clear correlation with the solids fraction value. This can be attributed to the random addition of noise, leading to random variations in pixel values. Furthermore, Tables S7 and S8 present additional findings regarding the noise level requirements. These tables provide information on the probability threshold necessary to ensure that the relative error of pixel values remains below a predefined threshold.

3.4. The effect of noise on bubble size measurements

Bubble size in fluidized beds, which is related to gas-solids contact efficiency, is an essential parameter for measuring fluidized bed characteristics [31]. The bubble size of a fluidized bed can be measured by the ECT sensor by first identifying if a bubble is present on the middle axial plane, then selecting a threshold to distinguish between the bubble and emulsion phases, and finally calculating the bubble size and associated characteristics. A detailed description of this process can be found in previous publications [14,32]. Therefore, the threshold selection is critical for

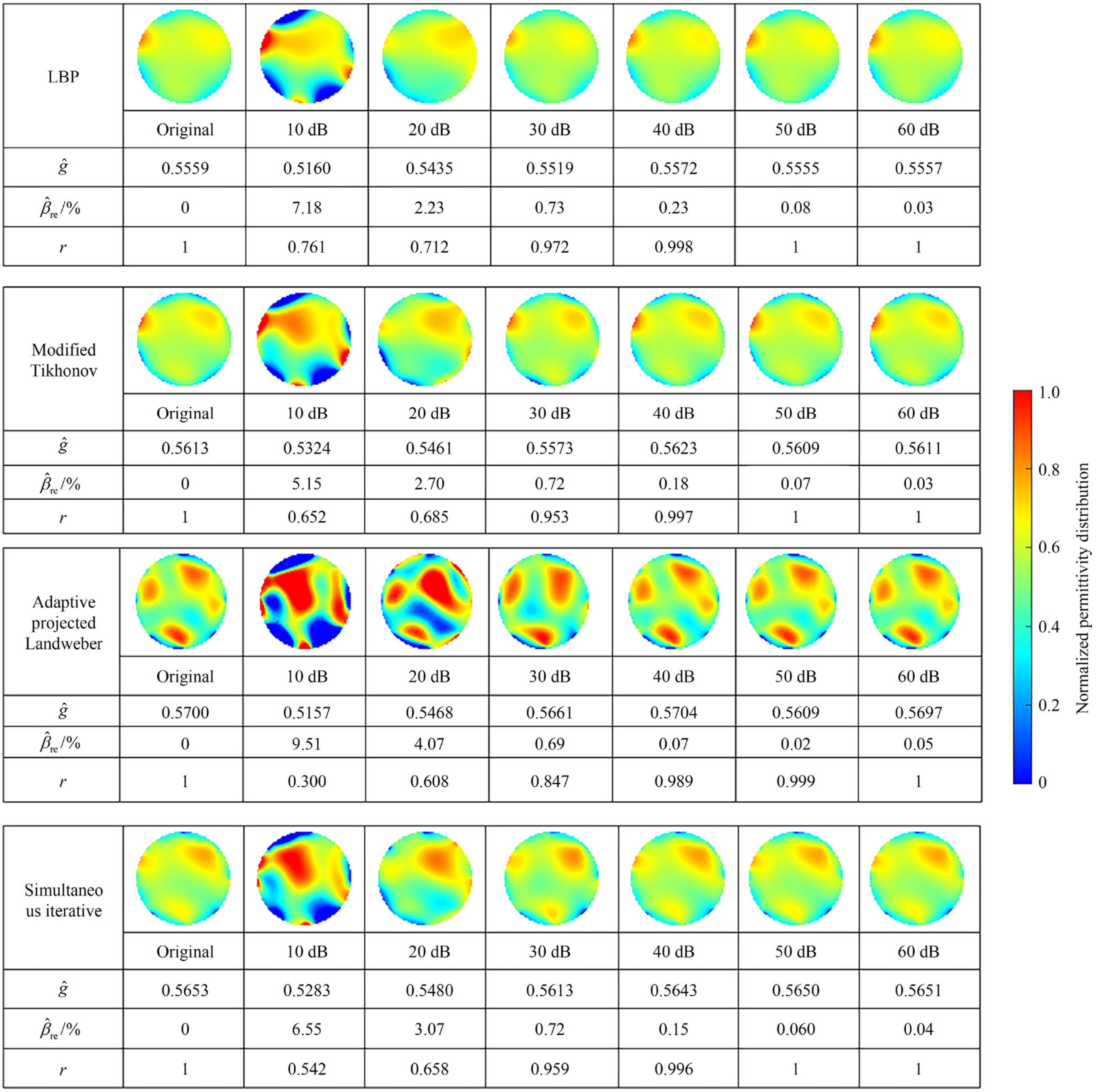

LBP	Original	10 dB	20 dB	30 dB	40 dB	50 dB	60 dB
$\hat{g}$	0.5559	0.5160	0.5435	0.5519	0.5572	0.5555	0.5557
$\hat{\beta}_{\mathrm{re}}$/%	0	7.18	2.23	0.73	0.23	0.08	0.03
r	1	0.761	0.712	0.972	0.998	1	1

Modified Tikhonov	Original	10 dB	20 dB	30 dB	40 dB	50 dB	60 dB
$\hat{g}$	0.5613	0.5324	0.5461	0.5573	0.5623	0.5609	0.5611
$\hat{\beta}_{\mathrm{re}}$/%	0	5.15	2.70	0.72	0.18	0.07	0.03
r	1	0.652	0.685	0.953	0.997	1	1

Adaptive projected Landweber	Original	10 dB	20 dB	30 dB	40 dB	50 dB	60 dB
$\hat{g}$	0.5700	0.5157	0.5468	0.5661	0.5704	0.5609	0.5697
$\hat{\beta}_{\mathrm{re}}$/%	0	9.51	4.07	0.69	0.07	0.02	0.05
r	1	0.300	0.608	0.847	0.989	0.999	1

Simultaneous iterative	Original	10 dB	20 dB	30 dB	40 dB	50 dB	60 dB
$\hat{g}$	0.5653	0.5283	0.5480	0.5613	0.5643	0.5650	0.5651
$\hat{\beta}_{\mathrm{re}}$/%	0	6.55	3.07	0.72	0.15	0.060	0.04
r	1	0.542	0.658	0.959	0.996	1	1

Fig. 9. Reconstructed images with identical noise levels across four algorithms, based on a single ECT measurement. r is the correlation coefficient, and $\hat{\beta}_{\mathrm{re}}$ denotes the relative error.

bubble size measurements. Du *et al.* [25] summarized different methods for determining the threshold based on the probability density function (PDF) curves of local solids fraction time signals. In this work, we first investigated the impact of noise on the PDF curves of the local solids fraction time signals with limited noise effects. Fig. S16 displays the PDFs corresponding to designated ϕ as referenced in Table S7. As depicted in Fig. S16, it is evident that the constrained noise has minimal impact on the PDF curves. Consequently, distinguishing between the bubble and emulsion phases becomes more straightforward.

Recognizing the limited influence of constrained noise on the PDF curves, it is rational to infer that this noise also has little effect on fluidized bed characteristics, particularly in terms of discriminating between solids and bubbles, such as bubble recognition and bubble size measurements. To validate our assumption, we computed the normalized error of the bubble area to assess the noise effect on bubble size measurements, as shown in Eq. (13).

$$A_{\mathrm{re}} = \left|(A_{\mathrm{noise}} - A) / A_{\mathrm{column}}\right| \tag{13}$$

where A_{noise} and A represent the bubble area with and without noise effects, respectively, A_{column} is the area of the cross-section of measurement zones, which normalizes the comparison between different bubble sizes. We also obtained the requirement of the

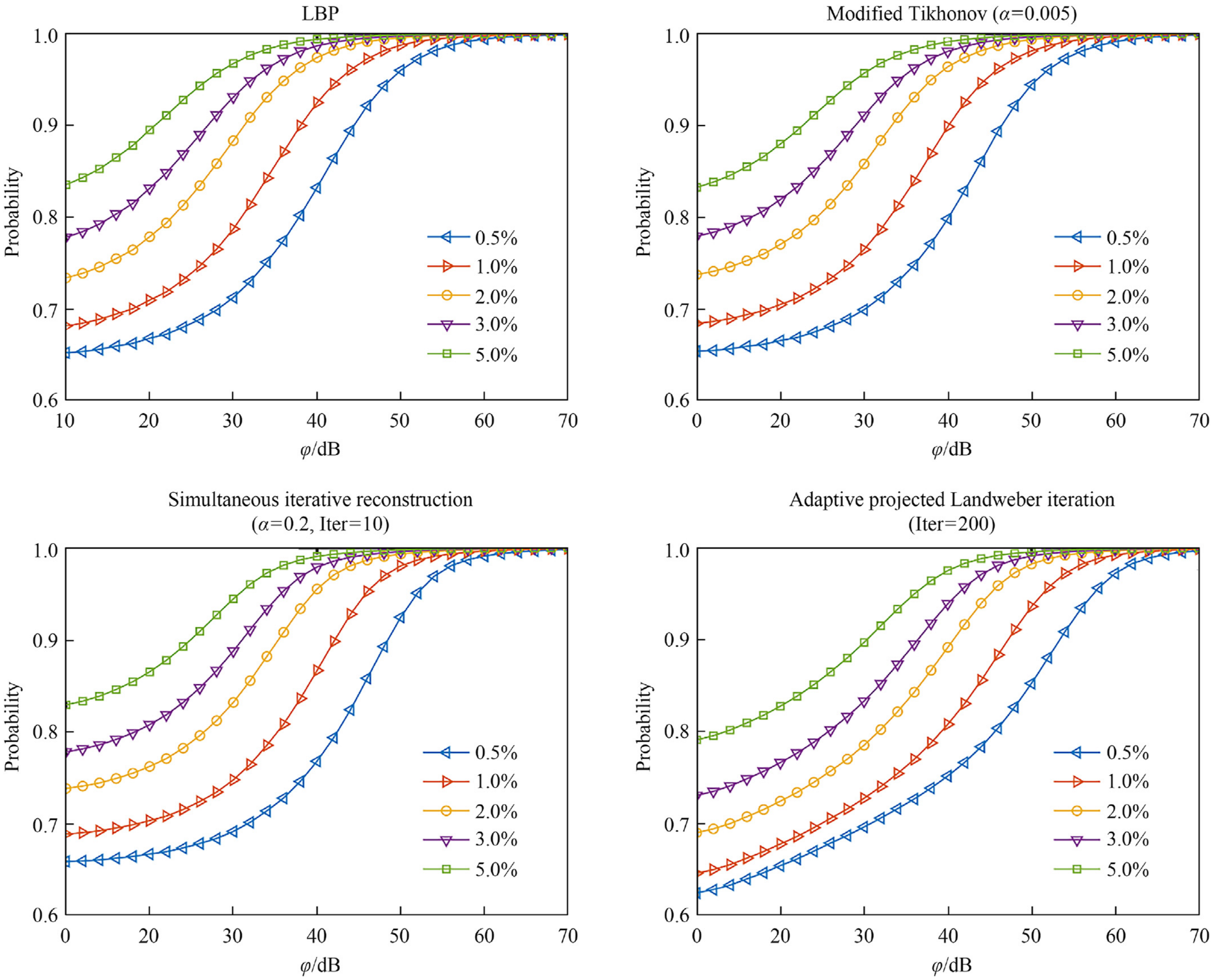

Fig. 10. Changes in the probability of ensuring the relative error of pixel solids fraction is smaller than designed thresholds with ϕ, with the 8-electrode ECT sensor and four algorithms.

probability of ensuring the normalized error of measured bubble size is smaller than designed thresholds with ϕ, as shown in Fig. 11.

Fig. 11 illustrates that the impact of noise on bubble size measurements diminishes with the increase in ϕ, and a higher ϕ is required for a stricter requirement of normalized error. It is also observed that the impact of noise on bubble size measurements is compromised compared to its effect on single pixel value measurements, consistent with the earlier discussion. Additionally, it is noted that the noise effect increases with the rise in algorithm complexity, aligning with the findings mentioned earlier. It is worth noting that the curves we obtained are not smooth. This is because, in the analysis of 50000 frames of data, there are approximately 1000 frames in which bubbles can be analyzed. However, this does not affect the overall trend. From another perspective, frames with bubbles consistently correspond to a lower average solids fraction and a higher fluctuation in solids fraction distribution, which reduces the noise effect on solids fraction distribution according to Fig. 7 and Fig. S9. Considering that bubble size measurements are based on the solids fraction distribution of that frame, the decrease in noise impact on bubble size measurements is also evident. We also presented the results of the effect of noise on bubble size measurements in the 12-electrode sensor, as shown in Fig. S17.

3.5. Relationship between noise effect and algorithm selection

When using ECT to measure the distribution of multiphase flow, the limited number of capacitance values compared to the reconstructed pixels allows us to obtain images that approximate the true distribution, leading to various algorithms developed to enhance accuracy and calculation speed [4,5]. However, due to the absence of true images, it is difficult to decouple the effects of algorithms and noise on the reconstructed images by comparing them to the true distributions. Similarly, the objective of this study is to simulate the impact of noise, commonly in real gas-solids fluidized bed measurements, on reconstructed images and other characteristics, compared to those obtained without noise interference under specific algorithms. Therefore, we referred to the work of Yang and Peng [4] and selected four different types of algorithms to examine the measurement reliability under specific algorithms and noise interference (compared to measurements without noise).

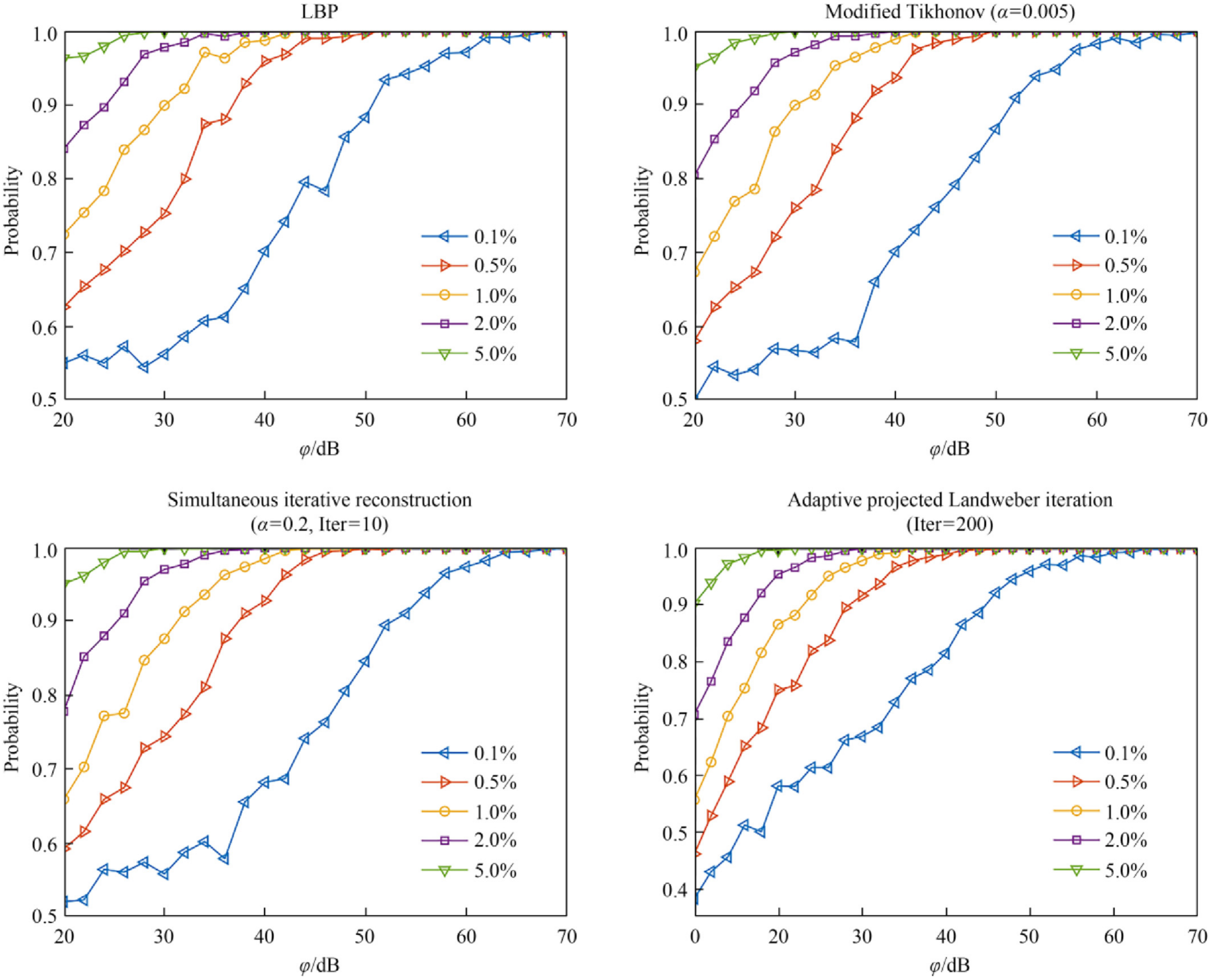

LBP

Modified Tikhonov (α=0.005)

Simultaneous iterative reconstruction (α=0.2, Iter=10)

Adaptive projected Landweber iteration (Iter=200)

Fig. 11. Changes in the probability of ensuring the normalized error of bubble size smaller than designed thresholds with ϕ, with the 8-electrode ECT sensor and four algorithms. Bubble threshold: 0.3.

Additionally, we obtained images based on these four algorithms with the same equivalent signal strength, using the same measurement capacitance vector, as shown in Fig. 9. By comparing these images, we gain a more intuitive understanding of algorithm selection and the effects of noise.

As shown in Fig. 9, the reconstructed images generated by different algorithms display noticeable variations. According to the previous studies, the modified Tikhonov, simultaneous iterative reconstruction, and adaptive projected Landweber algorithms achieve higher reconstruction accuracy than the LBP algorithm, with the adaptive projected Landweber algorithm producing images closest to the true distribution [27,33]. Moreover, all algorithms introduce distortions to the noise-free images when noise is present. As the ϕ increases (*i.e.*, as the noise level decreases), the impact of noise is progressively reduced, leading to noisy images that increasingly approximate the reconstructed images in the absence of noise.

Furthermore, it can be observed that as the complexity of the algorithm increases, particularly for the LBP and the adaptive projected Landweber algorithms (with the latter being a continued iteration of the former's results), the latter shows a greater distortion of the noise-free reconstructed images under the same noise intensity. This is primarily due to the iterative process further amplifying the impact of noise. We also obtained that the details in the reconstructed images become more pronounced as the complexity of the algorithms increases, leading to an increase in frame-based average solids fraction (average normalized permittivity).

4. Conclusions

In this work, the effect of noise on the performance of ECT for fluidized bed characteristics measurements was analyzed through statistical methods. The noise following the Gaussian distribution was added to the reference data at various levels. The ϕ, which defined the noise level, was used to evaluate the noise impact. This definition ensures that the results obtained can directly assess the ECT performances, given that ϕ equals the SNR of packed beds. The results demonstrate that the noise effects on accurately measuring the average solids fraction of individual frames are lower than those needed for accurately measuring solids fraction distributions and single-pixel values. This is because noise-induced fluctuations in the solids fraction of individual pixels are compromised when computing the frame average solids fraction. Furthermore, the 12-

electrode sensor requires a lower SNR (*e.g.* 10 dB lower) than that of the 8-electrode sensor to achieve the same accuracy in frame-based average solids fraction measurements. The fluctuation of solids fraction in fluidization usually reduces the SNR requirement (*e.g.* by 14 dB), especially with the adaptive projected Landweber algorithm. The impact of noise on bubble diameter measurement is relatively small. For 8-electrode and 12-electrode sensors, a SNR greater than 40 dB during the fixed bed phase ensures that the measurement error for bubble size remains below 2%. Consequently, the statistical analysis in this work can evaluate the noise effect on the measurement of fluidized bed characteristics and guide the design of ECT sensors in fluidized beds and other ECT measurements.

CRediT Authorship Contribution Statement

Kai Huang: Writing – review & editing, Writing – original draft, Visualization, Validation, Resources, Methodology, Investigation, Formal analysis, Data curation, Conceptualization. Chunlei Pei: Writing – review & editing, Visualization, Validation, Supervision, Resources, Project administration, Methodology, Investigation, Funding acquisition, Formal analysis, Data curation, Conceptualization. Shuanghe Meng: Resources, Investigation. Wuqiang Yang: Writing – review & editing. Hua Li: Software. Mao Ye: Writing – review & editing, Validation, Supervision, Resources, Methodology, Investigation, Formal analysis, Conceptualization. Jinlong Gong: Writing – review & editing, Visualization, Validation, Supervision, Resources, Project administration, Funding acquisition.

Data Availability

All the data supporting the findings of this study are available from the corresponding author upon reasonable request.

Declaration of Competing Interest

The authors declare that they have no known competing financial interests or personal relationships that could have appeared to influence the work reported in this paper.

Acknowledgements

We acknowledge the National Key Research and Development Program of China (2021YFA1501302), the National Natural Science Foundation of China (22121004, 22122808), the Haihe Laboratory of Sustainable Chemical Transformations and the Program of Introducing Talents of Discipline to Universities (BP0618007) for financial support. This work is supported by the XPLORER PRIZE.

Nomenclature

Symbols

A	bubble area
C	raw capacitance
g	normalized permittivity distribution of each frame
N	number of pixels
Q	number of frames
s	pixel area
β	solids fraction distribution of each frame
γ	correlation coefficient
θ	solids fraction distribution of packed bed
λ	normalized capacitance
σ	standard deviation
φ	equivalent signal strength

Superscripts and Subscripts

e	error due to the effect of noise
H	high-permittivity calibration
L	low-permittivity calibration
n	noise signal
noise	parameter with noise effect
ns	signal with noise effect
s	signal without noise effect
re	relative error with noise effect
-	time average
ˆ	average in reconstruction

Supplementary Material

Supplementary data to this article can be found online at https://doi.org/10.1016/j.cjche.2024.09.033.

References

[1] H. Wu, B. Buschle, Y.J. Yang, C. Tan, F. Dong, J.B. Jia, M. Lucquiaud, Liquid distribution and hold-up measurement in counter current flow packed column by electrical capacitance tomography, *Chem. Eng. J.* 353 (2018) 519–532.

[2] W. Warsito, L.S. Fan, Measurement of real-time flow structures in gas–liquid and gas–liquid–solid flow systems using electrical capacitance tomography (ECT), *Chem. Eng. Sci.* 56 (21–22) (2001) 6455–6462.

[3] Z.P. Wang, Q. Chen, X.Y. Wang, Z.H. Li, Z.X. Han, Dynamic visualization approach of the multiphase flow using electrical capacitance tomography, *Chin. J. Chem. Eng.* 20 (2) (2012) 380–388.

[4] W.Q. Yang, L.H. Peng, Image reconstruction algorithms for electrical capacitance tomography, *Meas. Sci. Technol.* 14 (1) (2003) R1–R13.

[5] Z.Q. Cui, Q. Wang, Q. Xue, W.R. Fan, L.L. Zhang, Z. Cao, B.Y. Sun, H.X. Wang, W. Q. Yang, A review on image reconstruction algorithms for electrical capacitance/resistance tomography, *Sens. Rev.* 36 (4) (2016) 429–445.

[6] P.N. Darma, M.R. Baidillah, M.W. Sifuna, M. Takei, Improvement of image reconstruction in electrical capacitance tomography (ECT) by sectorial sensitivity matrix using a *K*-means clustering algorithm, *Meas. Sci. Technol.* 30 (7) (2019) 075402.

[7] J. Kryszyn, D.M. Wanta, W.T. Smolik, Gain adjustment for signal-to-noise ratio improvement in electrical capacitance tomography system EVT4, *IEEE Sensor. J.* 17 (24) (2017) 8107–8116.

[8] L.J. Xu, H.L. Zhou, Z. Cao, W.Q. Yang, A digital switching demodulator for electrical capacitance tomography, *IEEE Trans. Instrum. Meas.* 62 (5) (2013) 1025–1033.

[9] E. Al Hosani, M.M. Zhang, M. Soleimani, A limited region electrical capacitance tomography for detection of deposits in pipelines, *IEEE Sensor. J.* 15 (11) (2015) 6089–6099.

[10] Z.Q. Cui, Y.X. Chen, H.X. Wang, A dual-modality integrated sensor for electrical capacitance tomography and electromagnetic tomography, *IEEE Sensor. J.* 19 (21) (2019) 10016–10026.

[11] M. Flatscher, M. Neumayer, T. Bretterklieber, Impedance matched electrical capacitance tomography system: front-end design and system analysis, *Meas. Sci. Technol.* 30 (10) (2019) 104002.

[12] Y. Li, D.J. Holland, Fast and robust 3D electrical capacitance tomography, *Meas. Sci. Technol.* 24 (10) (2013) 105406.

[13] Z. Zeeshan, C.E. Zuccarelli, D. Ospina Acero, Q.M. Marashdeh, F.L. Teixeira, Enhancing resolution of electrical capacitive sensors for multiphase flows by fine-stepped electronic scanning of synthetic electrodes, *IEEE Trans. Instrum. Meas.* 68 (2) (2018) 462–473.

[14] K. Huang, S.H. Meng, Q. Guo, W.Q. Yang, T. Zhang, M. Ye, Z.M. Liu, Effect of electrode length of an electrical capacitance tomography sensor on gas–solid fluidized bed measurements, *Ind. Eng. Chem. Res.* 58 (47) (2019) 21827–21841.

[15] S.N. Wang, J.M. Ye, Y.J. Yang, Quantitative measurement of two-phase flow by electrical capacitance tomography based on 3D coupling field simulation, *IEEE Sensor. J.* 21 (18) (2021) 20136–20144.

[16] M.T. Xie, H.M. Yang, K. Zhao, B.L. Yuan, J. Li, J. Liu, J. Ying, Y.S. Huang, J. Ou, Regularization parameter optimization based on the constraint of Landweber algorithm for electrical capacitance tomography, *Flow Meas. Instrum.* 69 (2019) 101620.

[17] Z.X. Liu, H.G. Wang, W.Q. Yang, R.H. Ge, Optimization of large scale concentric-annulus electrical capacitance tomography sensor with internal electrodes, *Measurement* 188 (2022) 110604.

[18] X.H. Hu, W.Q. Yang, Design of a data acquisition and function generation unit with USB, *Meas. Sci. Technol.* 17 (4) (2006) N17–N23.

[19] J.M. Ye, M.X. Mao, H.G. Wang, W.Q. Yang, Image reconstruction for ECT based on extended sensitivity matrix, *IEEE Sensor. J.* 16 (8) (2015) 2466–2476.

[20] Q. Guo, S.H. Meng, Y.F. Zhao, L.K. Ma, D.H. Wang, M. Ye, W.Q. Yang, Z.M. Liu, Experimental verification of solid-like and fluid-like states in the homogeneous fluidization regime of geldart A particles, *Ind. Eng. Chem. Res.* 57 (7) (2018) 2670–2686.

[21] W.Q. Yang, T.A. York, New AC-based capacitance tomography system, *IEE Proc. Sci. Meas. Technol.* 146 (1) (1999) 47–53.

[22] C. Tan, H.R. Jia, G.H. Liang, X. Wang, W.F. Niu, F. Dong, Combinational multimodality tomography system for industrial multiphase flow imaging, *IEEE Trans. Instrum. Meas.* 72 (2023) 4506610.

[23] Y.T. Makkawi, P.C. Wright, Fluidization regimes in a conventional fluidized bed characterized by means of electrical capacitance tomography, *Chem. Eng. Sci.* 57 (13) (2002) 2411–2437.

[24] N. Ellis, H.T. Bi, C.J. Lim, J.R. Grace, Hydrodynamics of turbulent fluidized beds of different diameters, *Powder Technol.* 141 (1–2) (2004) 124–136.

[25] B. Du, W. Warsito, L.S. Fan, Bed nonhomogeneity in turbulent gas–solid fluidization, *AIChE J.* 49 (5) (2003) 1109–1126.

[26] S. Fang, Y.D. Wei, L. Fu, G. Tian, H.B. Qu, Time-series analysis of the characteristic pressure fluctuations in a conical fluidized bed with negative pressure, *Chin. J. Chem. Eng.* 32 (2021) 87–99.

[27] Q. Guo, S.H. Meng, D.H. Wang, Y.F. Zhao, M. Ye, W.Q. Yang, Z.M. Liu, Investigation of gas–solid bubbling fluidized beds using ECT with a modified Tikhonov regularization technique, *AIChE J.* 64 (1) (2018) 29–41.

[28] S. Liu, L. Fu, W.Q. Yang, Optimization of an iterative image reconstruction algorithm for electrical capacitance tomography, *Meas. Sci. Technol.* 10 (7) (1999) L37–L39.

[29] W.B. Tian, J.T. Sun, M.F. Ramli, J.P. Wang, W.Q. Yang, An electrical capacitance tomography sensor with variable diameter, *IEEE Sensor. J.* 17 (7) (2017) 2089–2099.

[30] S.G. Liang, J.M. Ye, H.G. Wang, M. Wu, W.Q. Yang, Influence of the internal wall thickness of electrical capacitance tomography sensors on image quality, *Meas. Sci. Technol.* 29 (3) (2018) 035401.

[31] T. Wang, Z.H. Xia, C.X. Chen, Computational study of bubble coalescence/break-up behaviors and bubble size distribution in a 3-D pressurized bubbling gas–solid fluidized bed of Geldart A particles, *Chin. J. Chem. Eng.* 44 (2022) 485–496.

[32] C.E. Agu, C. Pfeifer, M. Eikeland, L.A. Tokheim, B.M.E. Moldestad, Models for predicting average bubble diameter and volumetric bubble flux in deep fluidized beds, *Ind. Eng. Chem. Res.* 57 (7) (2018) 2658–2669.

[33] G. Guo, G.W. Tong, L. Lu, S. Liu, Iterative reconstruction algorithm for the inverse problems in electrical capacitance tomography, *Flow Meas. Instrum.* 64 (2018) 204–212.